Progress In Electromagnetics Research M, Vol. 101, 219–239, 2021

On the Distortionless of UWB Wearable Hilbert-Shaped Metamaterial Antenna for Low Energy Applications

Ahmed I. Imran[1], Taha A. Elwi[2, *], and Ali J. Salim[1]

Abstract—This paper presents a miniaturized antenna-based wearable self-powered wireless systems; the proposed study identifies the possibility to compact a flexible Solant-Rectenna integrated to low energy devices. The proposed system uses the obtained DC currents from RF rectifier and solar panel to recharge batteries. A low-profile Hilbert-shaped metamaterial (MTM) array forming a rectangular patch is conducted to minimize the shadowing effects to 13.3% on the solar panel area. Nevertheless, an Electromagnetic Bandgap (EBG) square pads array is introduced as defects on the ground plane to remove the negative effects, in terms of losses, of the solar panel bus-bar on the antenna performance. Moreover, the proposed EBG ground plane is utilized to isolate the human body from the undesired electromagnetic radiation leakage in addition to minimize the antenna impedance mismatch caused by the proximity to human tissues. For this, the Specific Absorption Rate (SAR) is analysed numerically to assess the feasibility of the proposed EBG layer. The antenna shows a frequency bandwidth, $S_{11} < -10$ dB, from 0.8 GHz up to 10 GHz; moreover, the EBG inclusions increase the front to back ratio to provide the gains of -1 dBi, -4 dBi, dBi at 0.915 GHz, 1.88 GHz, and 2.45 GHz, respectively. Moreover, SAR reduction is achieved up to 64% down after the EBG layer introduction. The antenna distortion effect in terms of group delay (G_d) after 3.1 GHz up to 10 GHz is tested; the maximum variation is found to be less than 1 ns which shows a linear phase response with distortionless waveforms. Such a feature is found very suitable for UWB applications in modern wireless systems. The antenna performance improvement after introducing the proposed EBG defects is validated numerically and experimentally. The solar panel I–V characteristics are measured after the antenna structure introduction. Next, the solant RF port is connected to a rectifier circuit to realize the rectenna performance port that collects the RF energy at three bands in terms of efficiency spectra. Finally, it is proofed that the proposed Solant-Rectenna offers an excellent, compacted, and flexible candidate for the wearable self-powered devices at different bands.

1. INTRODUCTION

Nowadays microstrip antennas have become a research hotspot because of their unique characteristics such as low profile, conformability to mounting hosts, and ease of manufacturing [1]. However, it is well known that traditional microstrip antennas suffer from narrow bandwidth and moderate gain which limit their employment in modern wideband communication systems [2]. Recently, Federal Communications Commission (FCC) allocated the frequency spectrum from 3.1 GHz to 10.6 GHz for UWB applications appropriate for different low energy devices [3]. Numerous challenges arise to overcome the inherent limitations of conventional microstrip antennas to permit sufficient matching for UWB applications. For this, different techniques have been proposed to increase the antenna bandwidth such as etching slots aperture coupling, multilayer stacked patches, and proximity feeding [4].

Received 30 November 2020, Accepted 9 March 2021, Scheduled 22 March 2021
* Corresponding author: Taha Ahmed Elwi (taelwi82@gmail.com).
[1] Electrical Engineering Department, University of Technology, Baghdad, Iraq. [2] Communication Engineering Department, Al-Ma'moon University College, Baghdad, Iraq.

MTMs and EBG structures are proposed as the next approaches to enhance the microstrip performance as in [5–20]. For instance, split ring resonators (SRRs) were introduced in many applications to enhance microstrip antenna performance by suppressing surface waves on the patch at specific frequencies as in [5, 6]. EBG structures patterned either as metal patches or etched from ground planes were proposed in [7] to reduce surface wave diffractions from the substrate edges. MTM was also widely applied to electrically small antenna design, in order to reduce dimensions and obtain multiband operation with high radiation efficiency [8–10]. However, there are two fundamental constraints for resonant MTM structures: highly resonant structures [11] and high conductor losses [12]. Miniaturized antennas based fractal-shaped space filling curves were proposed to increase bandwidth matching and size reduction [13–16]. A microstrip antenna was proposed in [17] based on six spiral MTM unit cells and a printed dipole element supported by a rectangular slot truncated ground plane for biomedical applications. Another compacted UWB antenna was presented in [18] based on a multibranch T-shaped stub for frequency band notch reconfiguration. In [19], Hilbert curves of a fractal microstrip antenna using a coplanar wave-guide feed were proposed for multiband applications. In order to achieve broad bandwidth and high gain, a rectangular patch antenna composed of periodic array of MTM structures fed via strip-line and backed by defective ground plane was presented in [20].

In this paper, a further study is conducted on a Hilbert-shaped antenna structure and the EBG array was inspired from published work in [2] previously to be printed on a new type of substrates. The originality of this work lies in the use of such an antenna on flexible solar panel substrates. Therefore, the resulting antenna shows a UWB metamaterial-based rectenna for low energy applications to cover a large band from 0.8 GHz to 10 GHz, in order to be used in two different modes: In the first mode, when the antenna is mounted on a flexible solar panel substrate, an energy harvesting option is achieved. In the second mode, the antenna works as a UWB antenna according to the definition provided by the FCC. The proposed antenna design is also suitable for wearable applications. The basic element of the proposed antenna is a fractal Hilbert curve backed by square pads of an EBG array. Extensive numerical investigations are reported to illustrate the design methodology and performance of the proposed antenna. The fabricated prototype on the sola panel is constructed from silver nano-particles (SNPs) and tested experimentally to be compared against the simulated results. The antenna profile is found relatively small with dimensions of 28 mm × 32 mm × 2.5 mm. Moreover, the antenna provides a small shadowing area which is crucial for solar energy harvesting in self-powered wireless devices. The proposed antenna utilizes an excellent gain bandwidth product over the frequencies from 0.8 GHz up to 3.1 GHz to suit the applications of RF energy harvesting in the GSM, RFID, Wi-Fi,Wi-MAX, and WLAN bands. For the bands after 3.1 GHz up to 10 GHz, the antenna shows a distortionless feature that is very suitable for UWB applications in terms of receiving and transmitting in low energy devices.

2. ANTENNA GEOMETRY

The geometry of the proposed antenna is shown in Fig. 1. The maximum antenna dimensions are 28 mm in width and 32 mm in length. The patch is composed of 3×5 planar Hilbert elements printed on a flexible solar panel with a thickness of 2.5 mm. The fractal geometry is chosen as the third-order Hilbert curve in order to increase the effective current path length within $4 \times 4\,\text{mm}^2$ area and control the impedance matching at the desired resonant frequencies through the T-stub capacitive coupling as shown in Fig. 1(a). Moreover, the unitcell provides a small shadowing area which is essential for self-powered wireless devices [21] when it is printed on the solar cells. Consequently, the printed Hilbert curve area can be calculated from the following formulas:

$$A = L \times W \tag{1}$$

The Hilbert curve width (W) is equal to 0.2 mm, whereas the length (L) can be obtained by

$$L = \left(2^k + 1\right) S \tag{2}$$

where k is the fractal index, and S is the unit cell outer dimension that equals 3.3 mm. The total Hilbert length is 29.7 mm. Hence, the area of the Hilbert structure is approximately $5.94\,\text{mm}^2$. The areas of the T-stub and the outer frame are calculated directly from Fig. 1(b) to be $0.468\,\text{mm}^2$ and $0.4\,\text{mm}^2$,

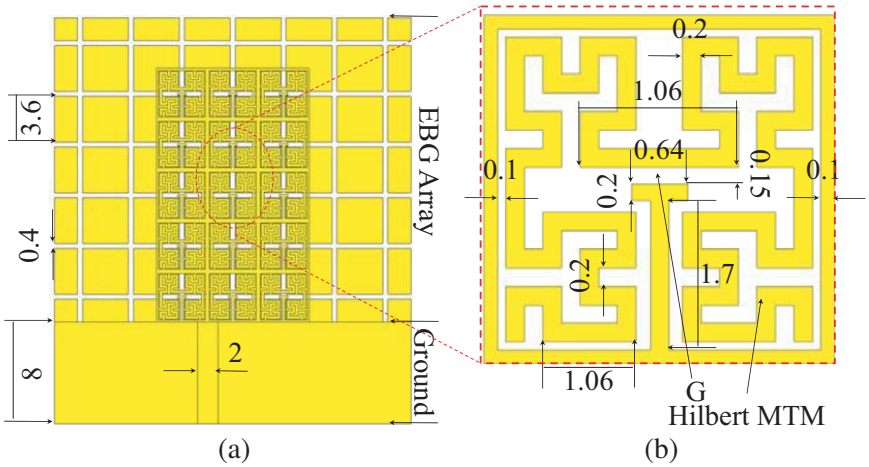

Figure 1. Geometry of the proposed Antenna; (a) Front view and (b) MTM unit cell.

respectively. By the summation of these three areas, the total effective area (A_{eff}) of individual unit cell is calculated to be 6.876 mm^2.

The patch area without considering the area of the feed line can be calculated by

$$A_{patch} = \sum_{1}^{m \times n} A_{eff} \tag{3}$$

where m and n are the 2D array dimensions of the proposed unit cells. Using Eq. (3), the patch area is found to be approximately 103 mm^2. Therefore, the total patch area to be printed on the solar panel reaches 119 mm^2 after including the feed line area which, in turn, is obtained based on the dimensions in Fig. 1(a). The percentage of the printed area that shadows the total used area from the solar panel is found to be approximately 13.3%.

It is worth to mention that the width of printed lines is fixed to 0.2 mm to ensure two points: minimizing the effective patch area to reduce the shadowing effects on the solar cell and to increase the radiated power as possible according to the following formula [2]:

$$P_{rad} = 94.746 \times w \times \left[1 - \text{sinc}\left(\frac{2L}{\lambda} 4\pi\right)\right] \tag{4}$$

where λ is the guided wavelength at the frequency band of interest. However, a fishnet-like transmission network shown in Fig. 1(a) ensures that the driving current excites each unit cell via couples energy to the unit cells. A 50 Ω off-centered microstrip line of 8 mm length and 2 mm width is used to feed the patch structure as shown in Fig. 1(a). To optimize the bandwidth of the equivalent solid patch, the ground plane defects based on EBG structures and the position of the feed line are selected. The loaded EBG defects on the ground plane are etched as square pads layer of 7×6 array as shown in Fig. 1(a). The details of the unit cell geometry are given in Fig. 1(b).

The basic element is reported by the approach outlined in [19], where different Hilbert orders were studied and presented to achieve the desired electromagnetic properties. However, in this paper, a patch structure based on the 3rd order Hilbert shaped unit cell is considered only. The width of the Hilbert line is selected to avoid unwanted cross-lines between the inner and outer traces due to the limited resolution of the printing process.

3. SOLAR CELL SUBSTRATE CHARACTERIZATION

This section discusses the reason behind introducing the EBG square pads array defects on the ground plane of the proposed antenna design. Such defects were not involved in the previous published designs in [5] and [19]. Flexible solar panels are usually constructed from polymer substrates with a conductive

bus-bar [22]. Therefore, the used solar panel is, firstly, characterized in terms of S-parameters as a substrate for a T-junction resonator to extract the effective losses. This resonator is used to measure the effects of the bus-bar on the antenna performance, to be constructed later, by retrieving the losses. The measurements are validated numerically using CST MWS [23]. Therefore, the proposed approach is suggested in this paper based on [24] to retrieve S-parameters. In this technique, a transmission line with a rectangular stub is etched on the front side of the solar panel as a T-junction resonator. The back side of the solar panel is covered with the defected EBG ground plane. The two sides of the T-junction resonator are soldered to two SMA ports of 50 Ω input impedance. All related geometrical details are given in Fig. 2 based on the numerical model. It is worth to mention that the solar panel polymer part has $\varepsilon_r = 3.5$ and loss tangent = 0.0027 [25].

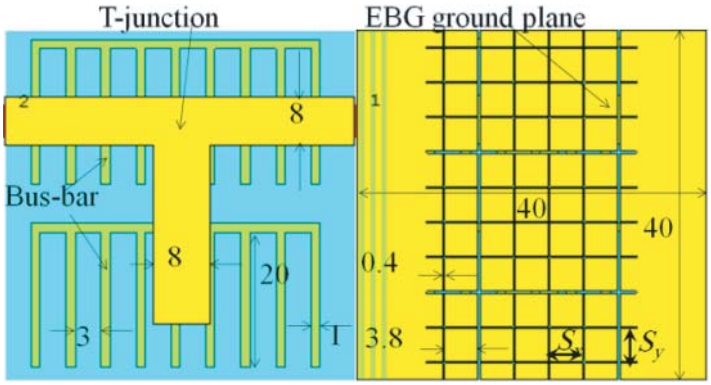

Figure 2. 3D structure of the T-junction transmission line.

For the discussed procedure, the S-parameters spectra are measured from Agilent 8720 vector network analyzer. The S-parameters are obtained from two cases based on a regular ground plane without EBG defects and with EBG defects as presented in Figs. 3(a) and 3(b), respectively. It can be noticed, from the obtained S-parameters in Fig. 3(a), that the model based on the regular ground plane provides less resonances than the case of introducing the EBG defects as shown in Fig. 3(b). This is attributed to the bus-bar layer losses which give rise to unrecognizable resonances [24]. However, after introducing the EBG layer, recognizable resonances are observed due to the EBG defects overcoming the bus-bar losses. Nevertheless, after calculating the losses spectra from the measured S-parameters of the two cases, see Fig. 3(c), it is found that significant losses are taken place due to the solar cell bus-bar structure which is impeded inside the polymer layer [25]. Such a layer may add significant conduction losses due to the inductive magnetization effects [24] that degrade the antenna performance. Moreover, the bus-bar layer may cause back antenna radiation leakage [25] that is not preferable in wearable devices. Therefore, it is found that the introduction of such EBG defects plays a major role in reducing the bus-bar loss effects by eliminating inductive part through the capacitive part of the proposed EBG layer [24].

Now, the MTM array when being mounted on the solar panel is characterized at the first Brillion zone (FBZ) with and without introduction of EBG defects to realize the propagation operation principle inside the used solar panel. It is found from Fig. 4(a) that the proposed MTM array provides a frequency bandgap between 15 GHz and 17.5 GHz when it is considered without the proposed EBG layer. However, the bandgap is shifted down between 1 GHz and 3 GHz after including the EBG structure. Such a change in the bandgap location is attributed to the change in the direction of the surface current motion on the MTM patch from the x-axis to the y-axis as shown in Fig. 4(b). Thus, the surface current along the patch length, y-axis, is subjected to a high attenuation due to the stopband effects as illustrated in Fig. 4(a), while the current along the x-axis is subjected to less attenuation.

Currently, the principle of operation of the proposed antenna is described in two significant rejoins. The antenna provides less attenuation along the x-axis for the combined EBG and MTM rejoins, while the attenuation is significant at the EBG rejoins. The proposed unit cell combination (EBG and MTM) now creates a propagation difference beyond the edge of the antenna patch; this allows

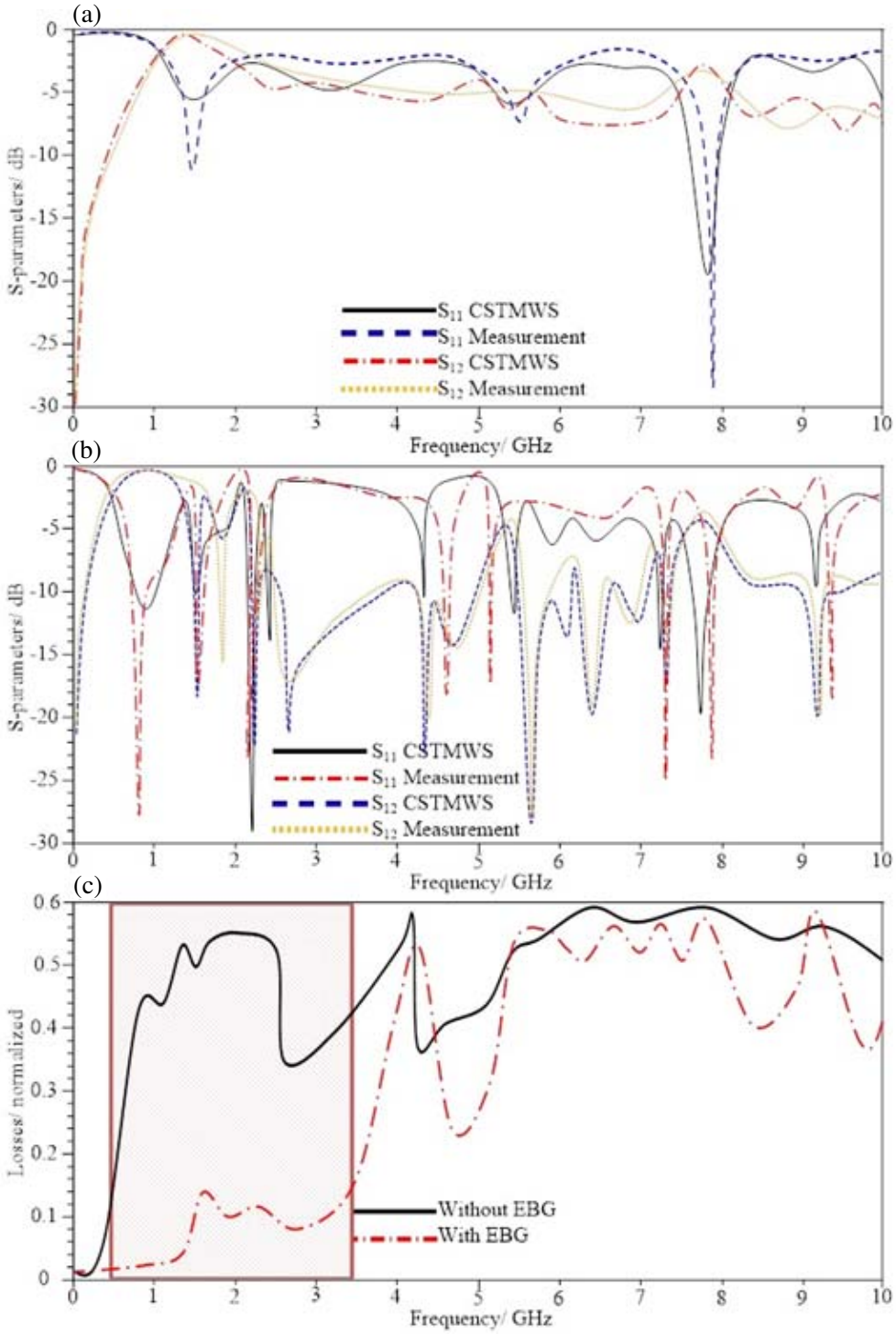

Figure 3. Evaluated losses based T-junction transmission; (a) S-parameters of the T-junction transmission without EBG structure, (b) S-parameters of the T-junction transmission with EBG structure, and (c) computed losses from the two proposed scenarios.

the current intensity at the ends of the patch to increase, as shown in Fig. 4(b). Such a combination therefore produces two distinct media at the patch edges with different electromagnetic properties to support antenna gain enhancements by suppressing surface waves [12]. In addition, it is found that the

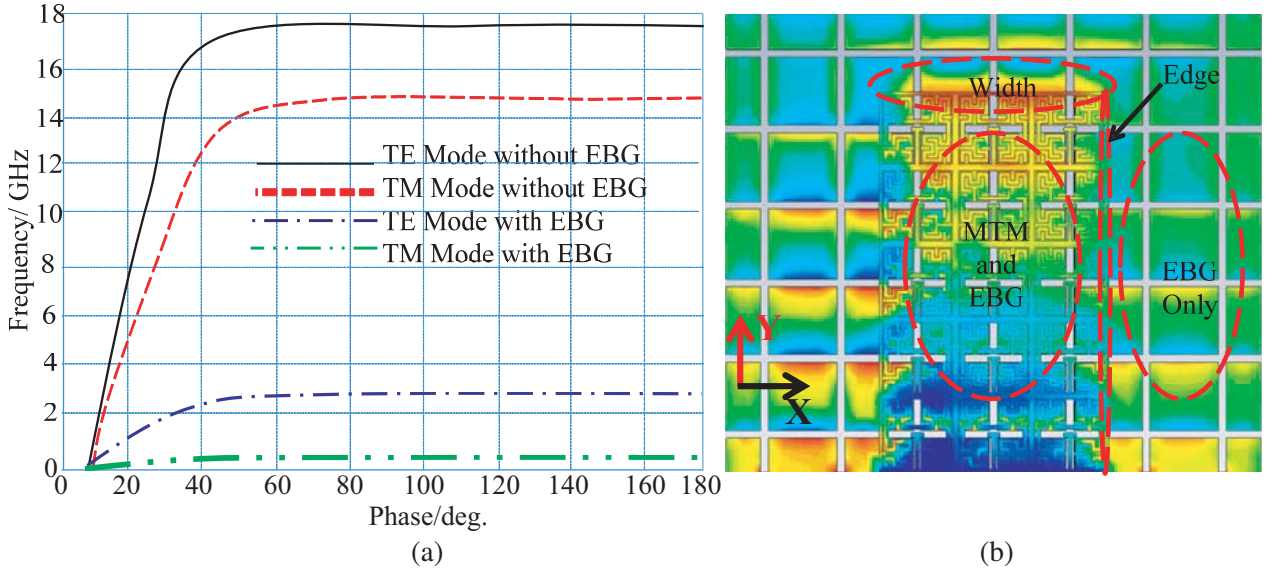

Figure 4. MTM unit cell performance; (a) Dispersion diagram of the proposed MTM unit cell at the FBZ and (b) surface current distribution.

proposed unit cell combination is anisotropic in structure that supports the current motion over the y-axis component along the x-axis.

From Fig. 4(a), the resultant difference in the band gap due to the bus-bar losses and coupling with the unit cell parts can be further explained by introducing the circuit realization based on Transmission Line Model (TLM) as shown in Fig. 5(a). The T-stub is presented by the $L_T C_T$ loop. The fractal part is represented by the series combination of $L_F C_F$. The junction between the EBG layer and MTM structure is characterized by the series branch of $L_P C_{EBG}$. The bus-bar part consists of the parallel branch $L_{SP} C_{SP}$, while R_{SP} and G_{SP} represent the solar panel losses. The coupling between the unit cell and the bus-bar is represented by the $C_C L_C$ branch. The values of the circuit lumped elements are evaluated and listed in Table 1 according to the geometrical formulations in [12]. Fig. 5(b) presents a comparison between the simulated results in terms of S-parameters based on an analytical TLM with respect to the full wave numerical simulations of CST MWS and HFSS [26]. Therefore, to explain the reduction in the losses, Fig. 3(c), and the change in the band gap location, Fig. 4, TLM is invoked for validation.

Table 1. Evaluated lumped elements.

Parameters	Value	Parameters	Value
L_F	2.7 nH	C_{EBG}	0.2 pF
C_F	9.1 nF	L_P	1.1 nH
L_C	1.9 nH	R_{SP}	40 Ω
C_C	0.7 nF	L_{SP}	0.4 nH
C_T	1.1 pF	C_{SP}	1.2 pF
L_T	0.9 nH	G_{SP}	50 mS

In this model, the number of proposed EBG unit cells is recognized according to the propagation function, $\gamma(x, y)$, which is given by the 2D inverse Fourier transform as:

$$\gamma(xy) = \sum_{u=0}^{M} \sum_{v=0}^{N} \Gamma(u, v) e^{j2\pi\left(\frac{ux}{M} + \frac{vy}{N}\right)} \tag{5}$$

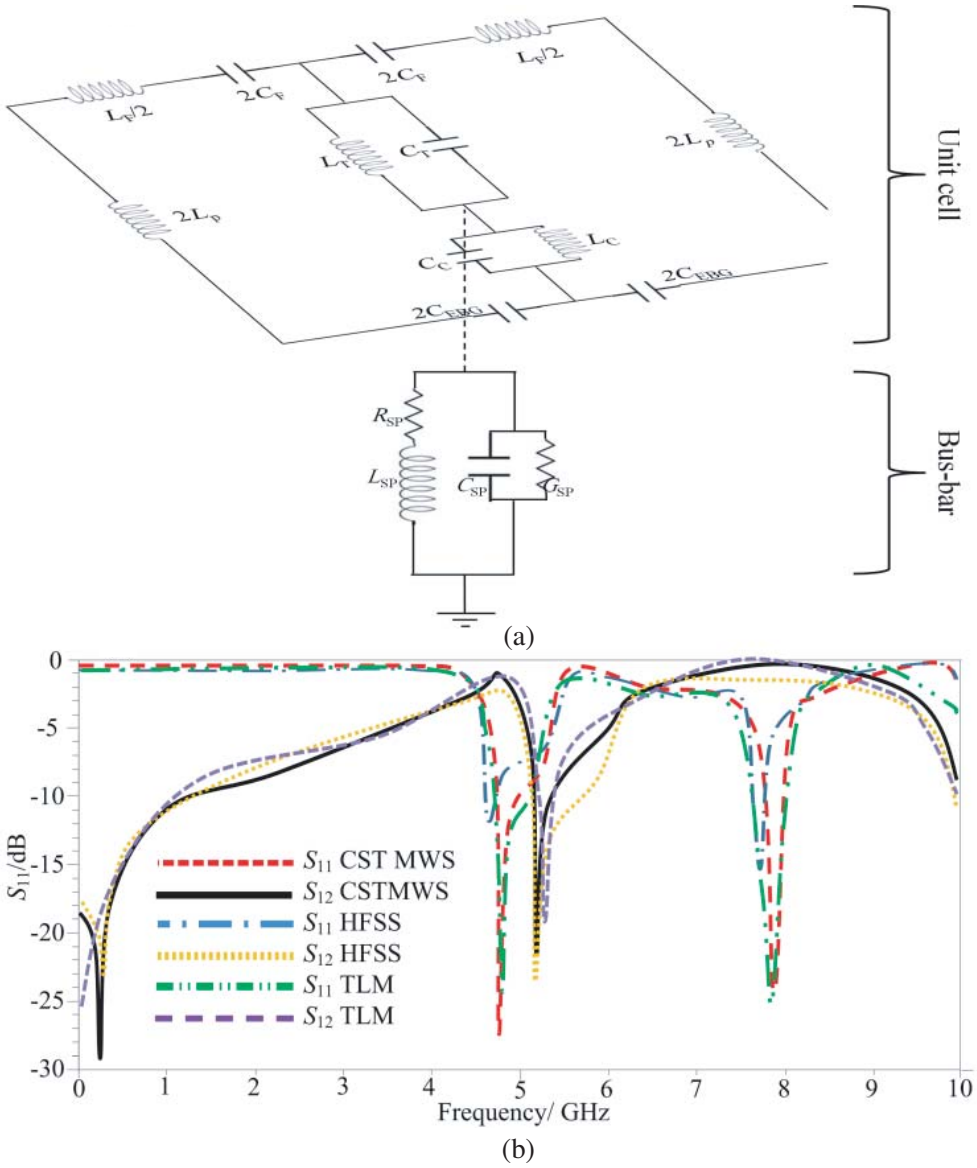

Figure 5. Unit cell properties based on the solar panel substrate; (a) Circuit realization based TLM and (b) evaluated S-parameters.

where M and N are the EBG array dimensions, and $\Gamma(uv)$ is the 2D propagation constant of an individual unit cell in the Fourier domain and given by:

$$\Gamma(u,v) = \sqrt{\Gamma_u^2 + \Gamma_v^2} \tag{6}$$

where u and v are wave numbers along the width and length, respectively, at the frequency band of interest. The propagation functions along u and v are derived from the Laplace inverse of the transmission line analyses which was discussed in [10]. Therefore, Γ_u and Γ_v are given by:

$$\Gamma_u = X \exp\left\{\sqrt{\left[R_F + j\omega(M\frac{L_{sp}}{L_T}L_C + L_F)\right]\left[\frac{G_{F+j\omega C_{EBG}}}{R_T G_T}\right]}\right\} p_x \tag{7}$$

$$\Gamma_v = Y \exp\left\{\sqrt{\left[G_{T+j\omega C_{EBG}}\right]\left[\frac{R_T + j\omega L_F}{NR_F G_F}\right]}\right\} p_y \tag{8}$$

where X and Y are the maximum array width along the x-axis and length along the y-axis, respectively. By satisfying the relative parameters from Table 1 and changing M from 1 to 6 as well as N from 1

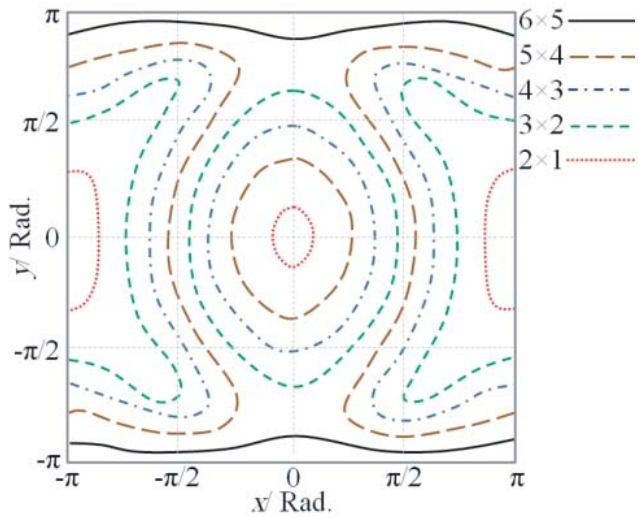

Figure 6. Propagation function, $\gamma(x, y)$, variation with different array indices.

to 5, the phase variation along the length (y) and width (x) is evaluated in Equation (5). However, due to the huge number of results that can be obtained from such parametric study, five cases are only considered for realizing $\gamma(x, y)$ as presented in Fig. 6 to reach the study satisfaction. From these results, it is found that considering the EBG layer based on 6×5 array, the propagation is maximized at the array edges at a distance away from the center which explains the current concentration on the patch edges, seen in Fig. 4(b).

4. DESIGN METHODOLOGY

The procedure of the proposed antenna design, see Fig. 1, is presented in this section. Therefore, CST MWS is invoked to develop the design in three cases:

Case 1: The design is started from a solid patch.

Case 2: Square slots are etched from the patch in case 1 to create a fishnet-like transmission network.

Case 3: The square slots are filed with the proposed MTM structure.

All the proposed cases are excited with a 50 Ω microstrip line of 2 mm width. The microstrip line is designed to realize 50 Ω matching impedance over the frequency band of interest. In fact, this is calculated after retrieving the relative constitutive parameters from the T-junction technique, where the authors used the evaluated values from the experimental work to calculate the width of the feed line. Nevertheless, the ground plane is defected partially with the proposed EBG layer to maintain the quality of the RF feeding from the 50 Ω SMA port [5]. Moreover, the feeding point may be loaded with an additional capacitance from the EBG layer that enhances the antenna matching bandwidth [4]. The feed structure is located from the patch edge at the same point to prevent interruption with the operation of MTM [4], where the antenna is not fed at the corner to avoid the mismatching due to the high impedance at the patch edges. A polymer layer is considered as a substrate with an embedded conductive bus-bar to realize the solar panel structure. Fig. 7 shows the front views of the proposed patches. It should be noted that the slot width (p_x) and slot length (p_y) are fixed to 3.68 mm and 3.68 mm, respectively.

The S_{11} spectra are evaluated using CST MWS. It is found that, for all proposed cases, the antenna shows wideband widths as shown in Fig. 8. Such observation is attributed to the effects of the capacitive coupling between the antenna patch and EBG defects [22]. However, case 3 shows the maximum enhancement due to the introduction of the MTM that tunes the frequency band towered lower frequencies. Nevertheless, the antenna gain spectra are also affected by introducing the MTM unit cells. For this, in case 3, the antenna offers a significant gain enhancement, see Fig. 8, progressively over

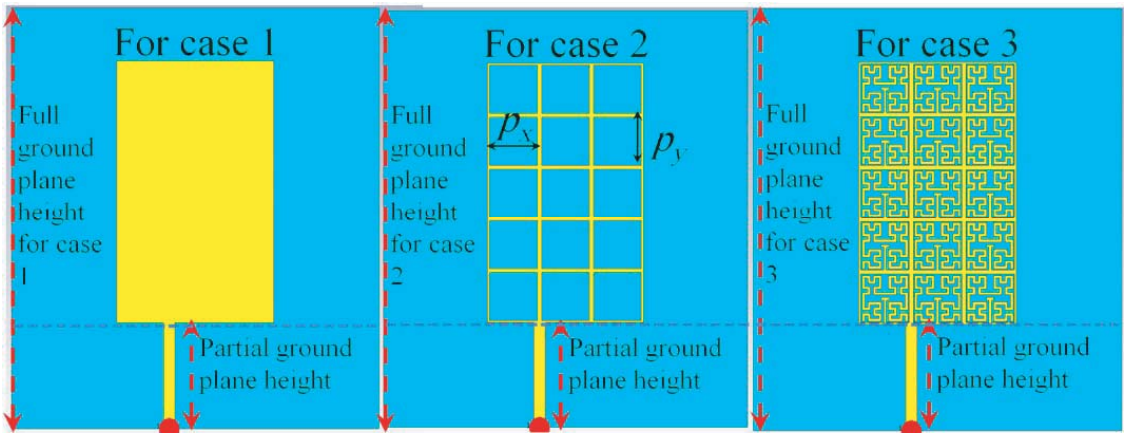

Figure 7. Numerical models of the proposed patches.

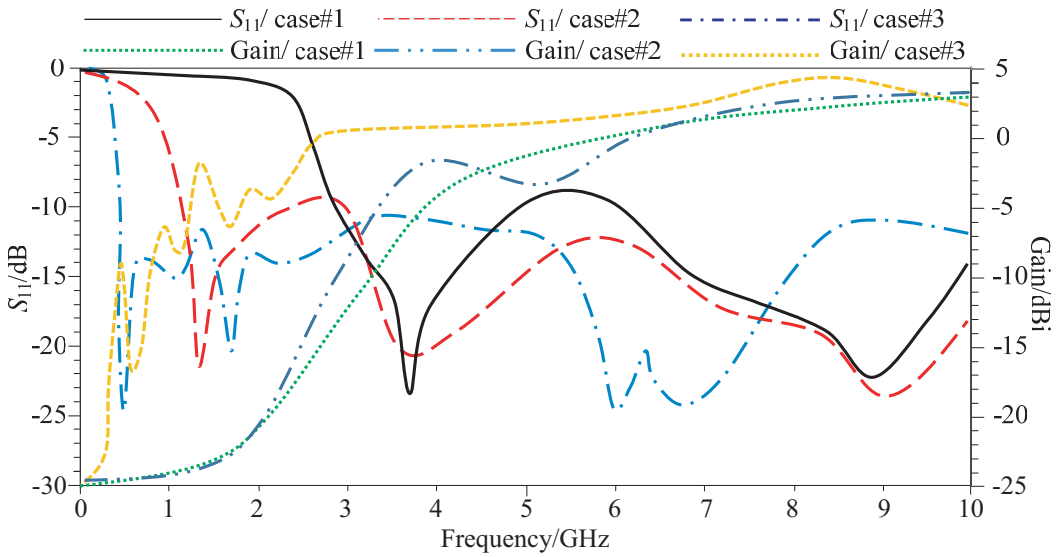

Figure 8. Simulated S_{11} and gain spectra based on the considered cases.

a wide band of frequencies. Such gain enhancement is attributed to the reduction in the capacitance effects between the patch and ground plane structures [22]. It is important to emphasize that case 3 offers wider bandwidth than in cases 1 and 2. This is attributed to the introduction of EBG defects which, due to fringing effects and diffraction from the substratum edges, achieve a significant reduction in surface waves [8]. Therefore, the antenna quality factor is reduced because of the dominance of the capacitive part over the inductive components of the ground plane [1], while the antenna bandwidth is improved.

5. PRINTING PROCESS

Flexible polycrystalline silicon, polymer, solar panel with an effective area of 8.4 cm × 6.0 cm and 2.5 mm thickness is used as a substrate, which reduces the effective ratio of the printed area to 2.36%. The solar panel is made of hydrophobic materials, in which the surface is not adhesive; therefore, the printing process without surface treatment is unfeasible. Therefore, an attempt of treating the solar panel surface using a plasma or chemical surface treatment leads to an efficient hydrophobicity reduction. Furthermore, the high temperature of the curing process may damage the material of the solar panel.

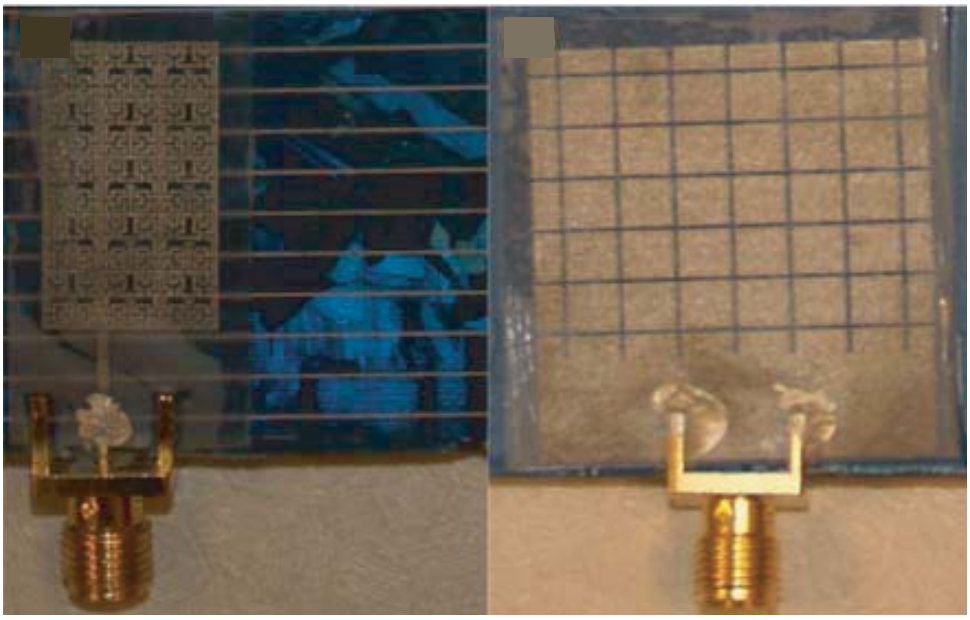

(a) (b)

Figure 9. Fabricated Solant-Rectenna: (a) Front view and (b) back view.

Consequently, the patch and ground plane are printed on a clear sticker paper. The specifications of this paper have thickness with 50 µm whose surface is transparent and highly adhesive. The patch layer is stacked on the upper surface of the solar cell, and the ground plane layer on the lower surface as can be seen in Fig. 9. For the connection of the 50 SMA port with the ground plane and the patch via the transmission line, Silver Paste is used.

6. SOLANT-RECTENNA MEASUREMENTS

The integration of printed circuit antennas into solar panels has been investigated in [22, 24, 25]. In [22], a microstrip patch antenna based on two solant designs was presented for GPS and S-band beacon transmission applications. A square patch antenna in [24] was reported for satellite communication systems. In [25], a dipole antenna mounted on a solar panel was reported for UWB applications.

In this work, the gained DC currents from the solar panel and the rectified RF energy are used to charge batteries for wearable systems in the applications of smart clothes. Therefore, the measurements in the following sections are applied to the proposed solant-rectenna as follows.

6.1. Antenna Performance Measurements

The performance of the proposed antenna is tested when it is mounted in air and then close to a human body. The obtained measurements are compared against the simulated results from CSTMWS. Experimentally, S_{11} spectra and radiation patterns are measured for two scenarios in air and on a human body. The measured S_{11} over the frequency range from 300 kHz to 10 GHz is shown in Fig. 10. It is found that the S_{11} spectrum of the printed antenna on the solar panel, solant-rectenna, is slightly affected. This is because of the EBG-defects; the coupling effects of the human body with the patch structure are mainly insulated. However, the proposed prototype provides a bandwidth range from 0.8 GHz to 10 GHz.

The radiation patterns are measured on the human model in the E- and H-planes at 0.915 GHz, 1.88 GHz, and 2.45 GHz as presented in Fig. 11. It is found that the antenna radiation patterns are relatively directive to the broadside due to the reduction in the surface wave diffraction with employing the proposed EBG layer. For this, the proposed antenna gain values, when it is mounted on air,

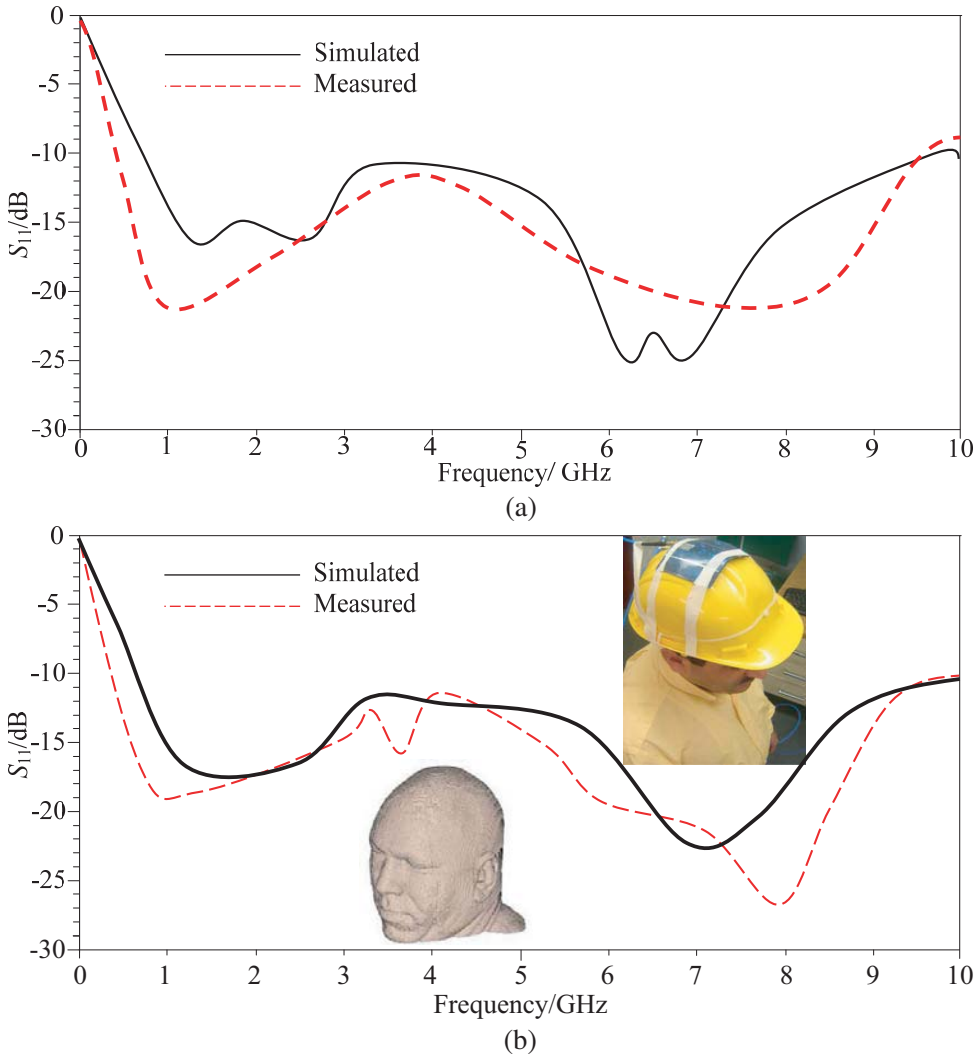

Figure 10. S_{11} comparison of the proposed antenna based measured and simulated results: (a) On air and (b) on human body.

are found to be −10 dBi, −4 dBi, and −0.1 dBi at 0.915 GHz, 1.88 GHz, and 2.45 GHz, respectively. However, when the antenna is close to the human body, it shows the gains of −10.2 dBi, −4 dBi, and 0 dBi at 0.915 GHz, 1.88 GHz, and 2.45 GHz, sequentially. The antenna maintains mostly the same gain with insignificant degradation due to the surface wave coupling isolation from the human head in the near-field [12].

6.2. Solant Performance

The measured I–V characteristics of the solar panel with and without the proposed antenna are seen in Fig. 12. During a sunny day, these measurements are performed in an outdoor environment. In both cases, the measured short circuit current at the 0 V input voltage is found to be 0.175 A. At the maximum input voltage, the measured open circuit current is found to be 1.1 mA. In addition, at a voltage step of 0.05 V (a value between maximum and minimum input voltages), the current produced from the solar panel, with and without the antenna proposed, is measured. It can be declared that the proposed antenna shows minor reduction in the produced current as can be seen in Fig. 12 because a small area of printing is used. Therefore, the objective of minimizing the shadowing effects due to the patch structure has been achieved successfully.

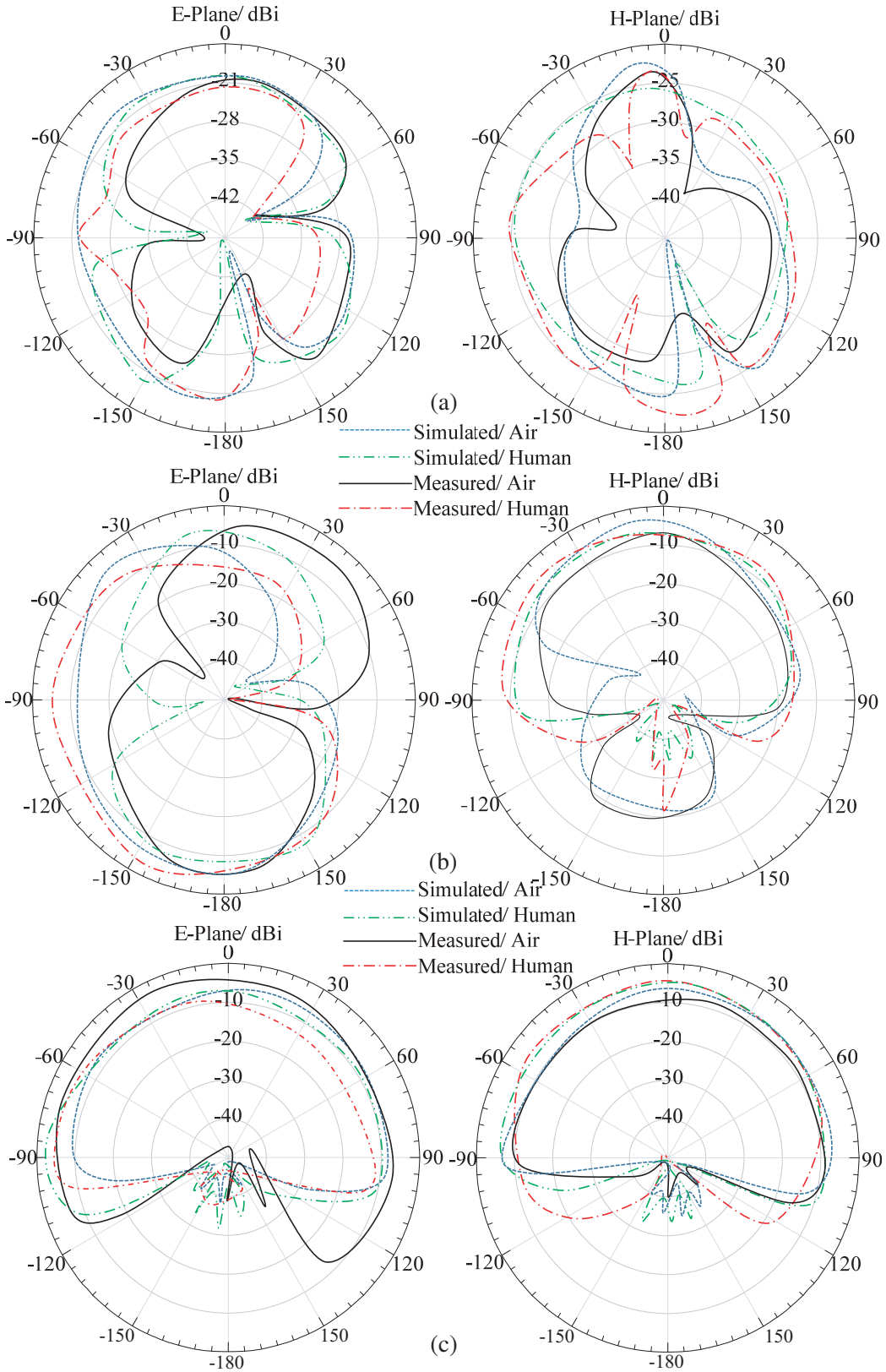

Figure 11. Far-field radiation patterns comparison between the two considered scenarios at E- and H-planes for: (a) 0.915 GHz, (b) 1.88 GHz, and (c) 2.45 GHz.

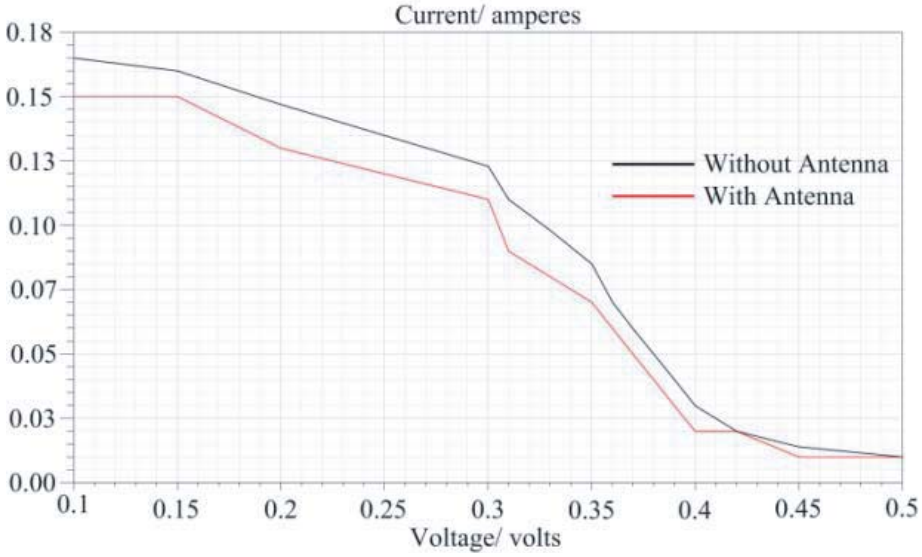

Figure 12. I–V characteristics measurements.

6.3. Rectenna Performance

After experimenting the solant performance, the RF energy harvesting measurements are conducted in terms of output DC voltage and conversation efficiency at 0.915 GHz, 1.88 GHz, and 2.45 GHz. The proposed antenna is connected to an RF Villard conversion module P21XXCSR-EVB evolution board with a matching circuit converting RF signals to DC output voltage at the three frequency bands of interest through a 50 Ω SMA port [27]. The RF harvester with HSMS 2860 Schottky diode chips is connected as a matching circuit between the rectenna load and the impedance of the circuit rectifier. The measurement setup involves three dipoles at the three considered frequencies to be located at 4 m from the proposed rectenna. The measurements are experimented inside an RF chamber to eliminate the interference from other outward sources. A digital oscilloscope monitors the measured conversion efficiency and the output DC voltage with respect to the transmitted power from the source, as shown in Fig. 13. At 0.915 GHz with a collected output DC voltage of 1.452 VV, the maximum conversion efficiency of the proposed rectenna is found about 90 %. The output voltage is found about 1.22 V with 49% at 1.88 GHz. The obtained efficiency at 2.45 GHz is found about 60% with an output voltage of 1.22 V. It is worth to mention that the proposed system is limited to a distance of 20 m away from the transmitter at 0.915 GHz; however, the distance reaches approximately 9 m and 4 m at 1.88 GHz and 2.45 GHz, respectively.

In Table 2, the proposed performance of Solant-rectenna is compared with other published literature results. In comparison to other published designs, the proposed antenna provides significant improvements in terms of reduction of size. Such enhancement is attributed to the addition of the EBG defects which realizes broadening in the radiation pattern and helps energy harvesting form different directions. Over the past similar designs, the main advantages of the antenna are the combination of two ports based on solar power and RF power in one integrated printed circuit. However, the flexible implementation of solar panels offers another feature to make integration with wearable and intelligent clothing designs easy. Nonetheless, The proposed antenna provides excellent frequency matching and accepted gain to cover Wi-Fi, Wi-Max, and Wi-Fi applications. Moreover, the proposed antenna in comparison to other published results shows the minimum shadowing effects on the solar panel. Finally, the proposed antenna offers a good matching capability, even when it is close to the human body.

It is worth to mention that the two DC current sources realized by the proposed Solant-rectenna can be combined through parallel connection of switched-mode technique [24]. Therefore, to achieve a reliable form of different source redundancy, two power supplies ports are connected in parallel with two diodes. Such connection prevents the possibility of short circuit occurrence and stops a fault current from flowing back into the defective power supply unit if one of the ports fails [28].

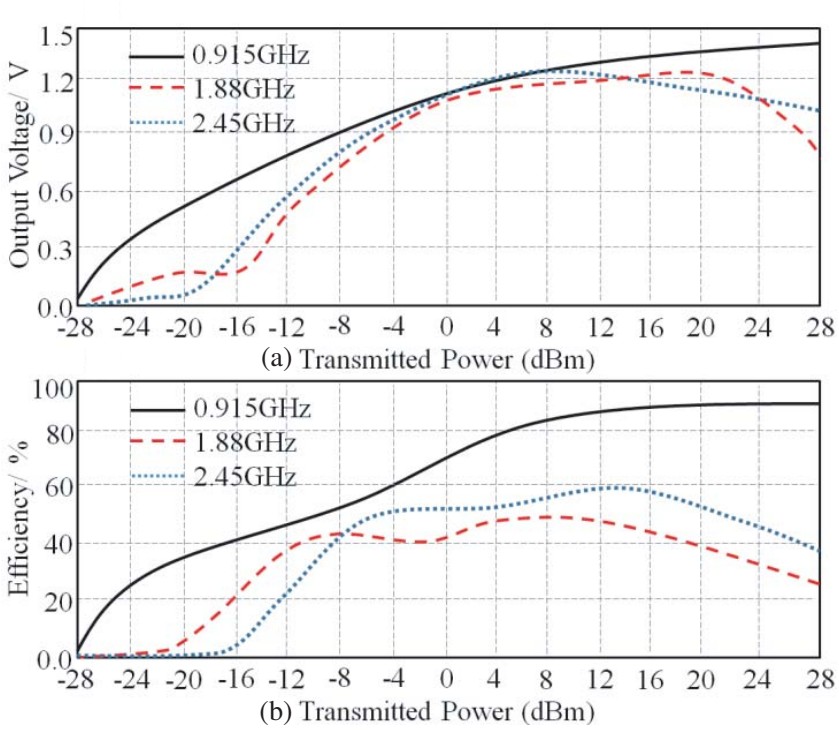

Figure 13. Solant-Rectenna performance: (a) Output voltage and (b) conversion efficiency.

Table 2. Achieved results with respect to published results.

References	Size (mm^2)	f/GHz	G_o/dBi	Type	V_{out}/V	η
5	32×28	2.45	1.9	Rectenna	0.0022	0.8
17	70×42	2.45	6.2	Rectenna	3.1	0.83
19	32×28	2.45	2.2	Rectenna	2	0.80
19	32×28	5.8	2.48	Rectenna	2.5	0.91
3	180×15	2.45	7	Rectenna-Array	11	0.65
4	200×200	2.45	9	Rectenna-Array	7	0.66
20	180×180	2.45	6	Solant-Array	0.35	–
21	160×160	4.14	3.2	Solant-Array	0.82	—
22	384×64	3.8	11.6	Solant-Array	7	—
25	800×200	0.9	2	Solant-Rectenna-Array	$V_{rectenna} = 12.45$ $V_{solant} = 14$	0.4
Proposed work	32×28	0.915	-10	Solant-Rectenna	$V_{rectenna} = 1.452$ $V_{solant} = 0.5$	0.9
		1.88	-4		$V_{rectenna} = 1.22$ $V_{solant} = 0.5$	0.49
		2.45	0		$V_{rectenna} = 1.22$ $V_{solant} = 0.5$	0.6

6.4. EBG Effects

In this section, the effects of the EBG defects on the antenna performance are discussed in terms of S_{11}, gain, front-back-ratio (F/B), and radiation efficiency (η_r) spectra. The obtained numerical results are measured experimentally for validation as seen in Fig. 14. The proposed antenna performance is significantly enhanced after the EBG structure introduction that justifies the difference with respect to the antenna design in [19]. Moreover, the antenna performance in [19] is compared to the proposed antenna. Such a comparison is exemplified to realize the advantages of adding the proposed EBG defects to the inspired patch. In Table 3, the main antenna performance is compared to realize the obtained advantages of adding the EBG structure. The proposed antenna shows a front to back ratio (F/B) to be 11.2 dBi, while F/B of the antenna in [29] is found to be 3 dBi. Moreover, the maximum antenna gain is approximately 4.55 dBi at 8.7 GHz and for the antenna in [19] is found to be 3.45 dBi at 9.2 GHz.

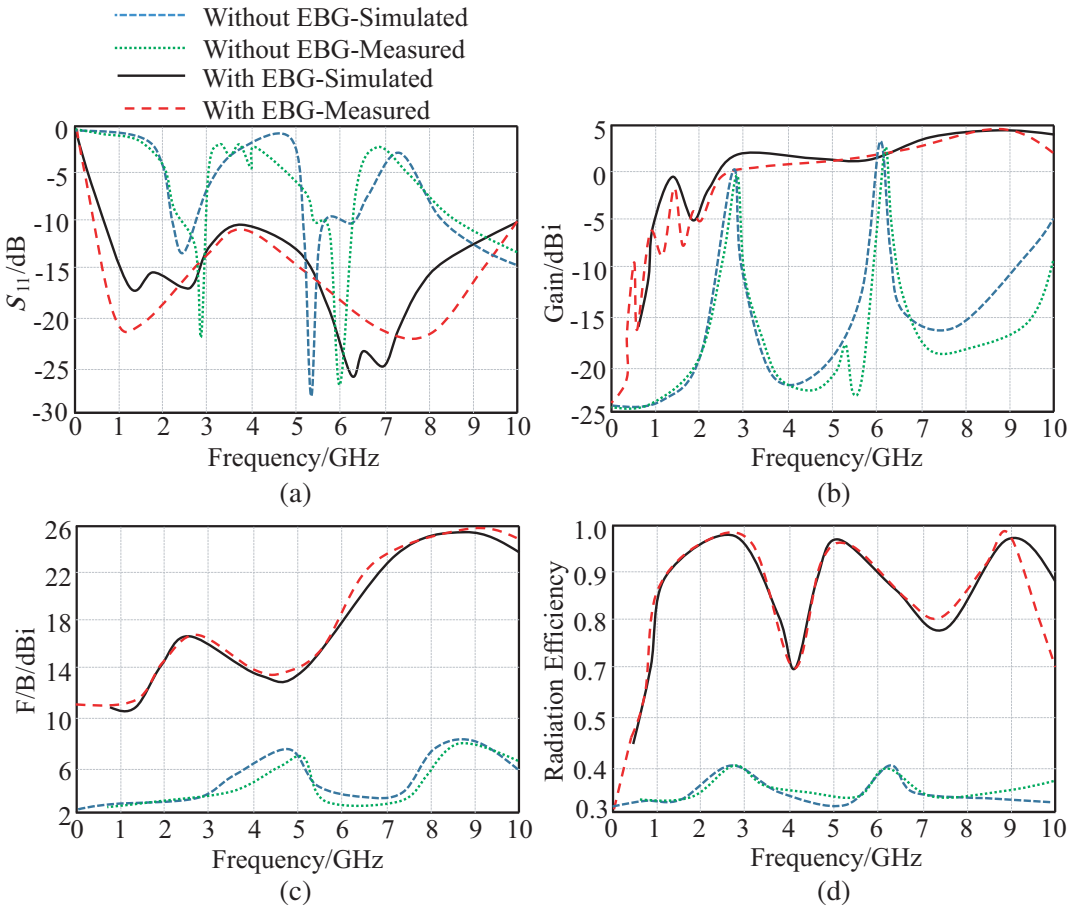

Figure 14. EBG effects on the proposed Solant-Rectenna performance: (a) S_{11}, (b) gain, (c) F/B, and (d) η_r.

Table 3. Comparison between the proposed antenna performances with a previous work in [19].

Ref.	BW/GHz	Gain/dBi	η_r	F/B/dBi	S_{11}/dB
Conventional [19]	2.4–10	−3 to 3.45	0.25 to 0.45	3 to 6	< -10
Proposed antenna	0.8–10	−11 to 4.55	0.64 to 0.95	11.2 to 25.2	< -20

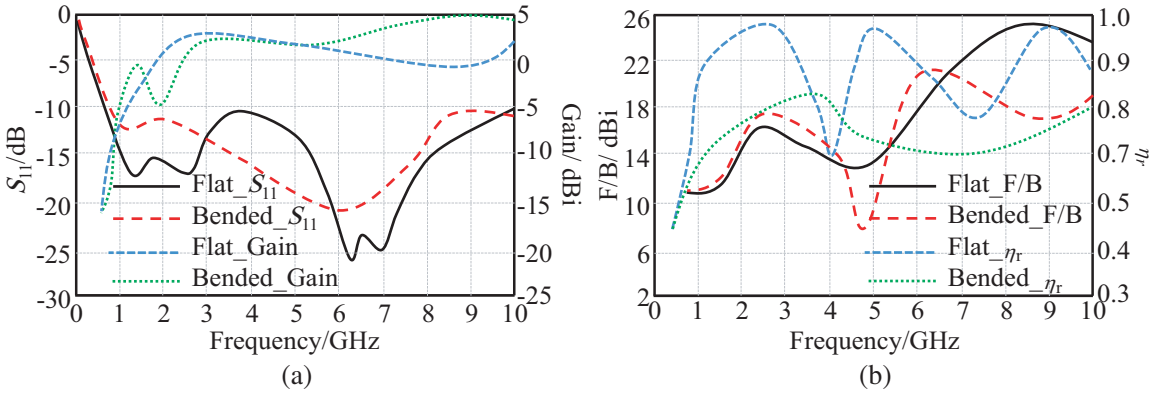

Figure 15. Bending effects on the proposed Solant-Rectenna performance: (a) S_{11} and gain, (b) F/B and η_r.

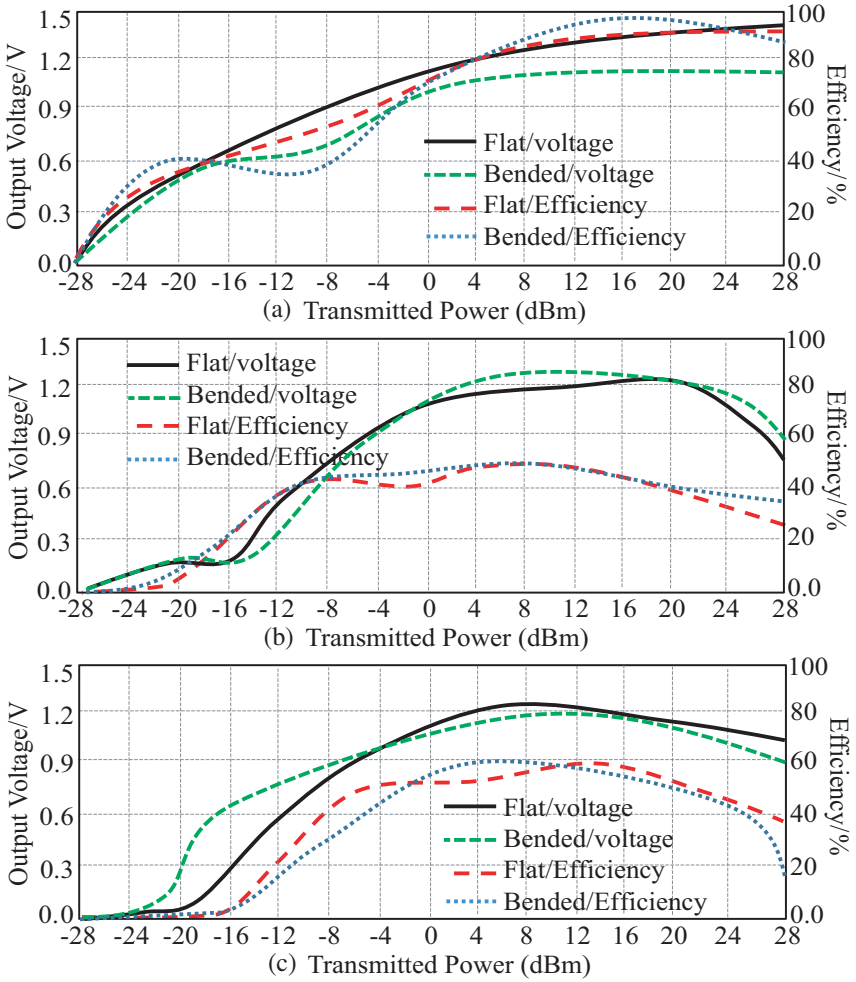

Figure 16. Bending effects on the rectification performance: (a) Output voltage and (b) conversion efficiency.

6.5. Bending Effects

The effects of bending on the proposed antenna are studied in this section. As seen in Fig. 15, S_{11} and gain spectra are unaffected significantly. This is attributed to the EBG layer introduction that

maintains the surface current motion [17]. However, F/B and η_r are affected by the antenna bending due to the change in the effective dielectric properties of the substrate [29].

The authors conducted this study to realize the effects of bending on the harvested RF energy in terms of V_{out} and η_r in Fig. 16. Insignificant bending effects are observed at the frequency bands of interest due to maintaining the S_{11} and gain spectra without effective changes.

6.6. Distortion Effects

The distortion effect in terms of (G_d) spectra from 3.1 GHz to 10 GHz is measured. This is due to operating the proposed antenna to receive and/or transmit information over UWB systems from 3.1 GHz to 10 GHz. Fig. 17 can be analyzed in two cases as follows:

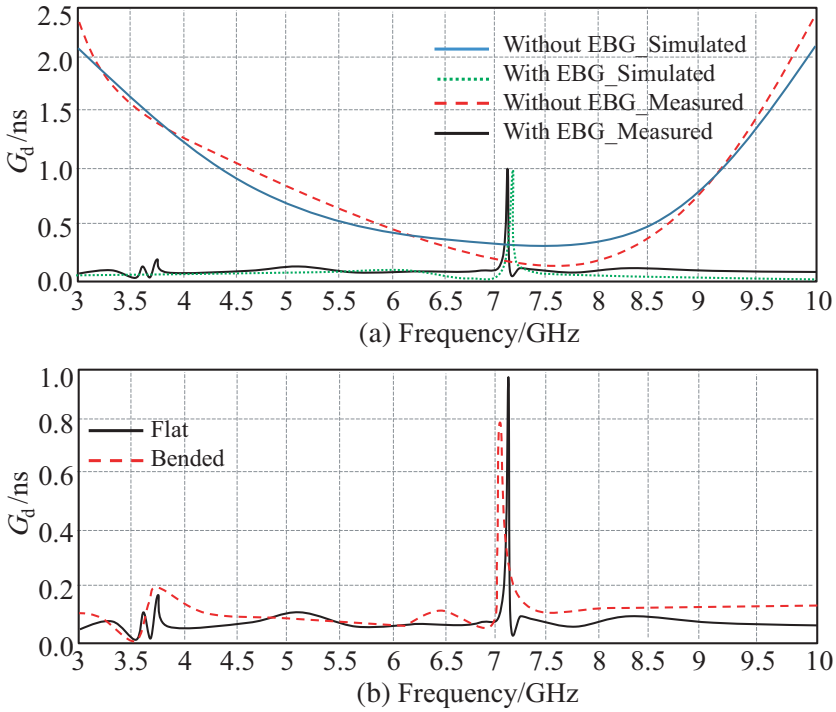

Figure 17. Group delay spectra: (a) With and without EBG defects and (b) with and without bending.

Case 1, introducing the EBG defects: it is found that the maximum variation occurs at 7.2 GHz with G_d not exceeding 1 ns to show a linear phase response over the entire UWB. This is to maintain a distortionless waveform in many modern applications.

Case 2, no EBG defects: the antenna suffers from a sever change in the G_d spectrum that limits the use in the UWB applications. The main reason of G_d variation is attributed to the solar panel bus-bar layer.

Therefore, it can be concluded from Fig. 17(a) that adding such EBG defects can remove the negative effects of the solar panel on antenna distortion spectrum.

The measurement is extended to realize the effects of bending on the group velocity as seen in Fig. 17(b). It is found that the group velocity is insignificantly affected, due to adding the proposed EBG layer that shows excellent ability of maintaining the antenna performance over a wide range of frequencies [4].

The authors summarized the main differences between proposed antenna features and that for most other relative published researches in Table 4. It is found that only the proposed antenna shows no significant distortion over a UWB flexible antenna with RF and solar energy harvesting features.

6.7. Considerations of SAR Effects

The SAR value is evaluated numerically at the three frequency bands of interest. Then, an experimental validation is conducted to realize the effective radiation leakage values. The quantity of SAR, given by absorption results on the head of the HUGO model inside CSTMWS environments, is presented in Fig. 18. In the proposed scenario, the wearable antenna device is considered to be mounted on a head helmet, particularly on the HUGO head part at a distance of 25 mm away from the head. To realize the radiation absorption inside the human body, the resolution of the HUGO model is considered to be 1 mm^3. As seen in Fig. 18, the SAR quantity is approximately 1.51 W/kg at 0.915 GHz and 1.26 W/kg

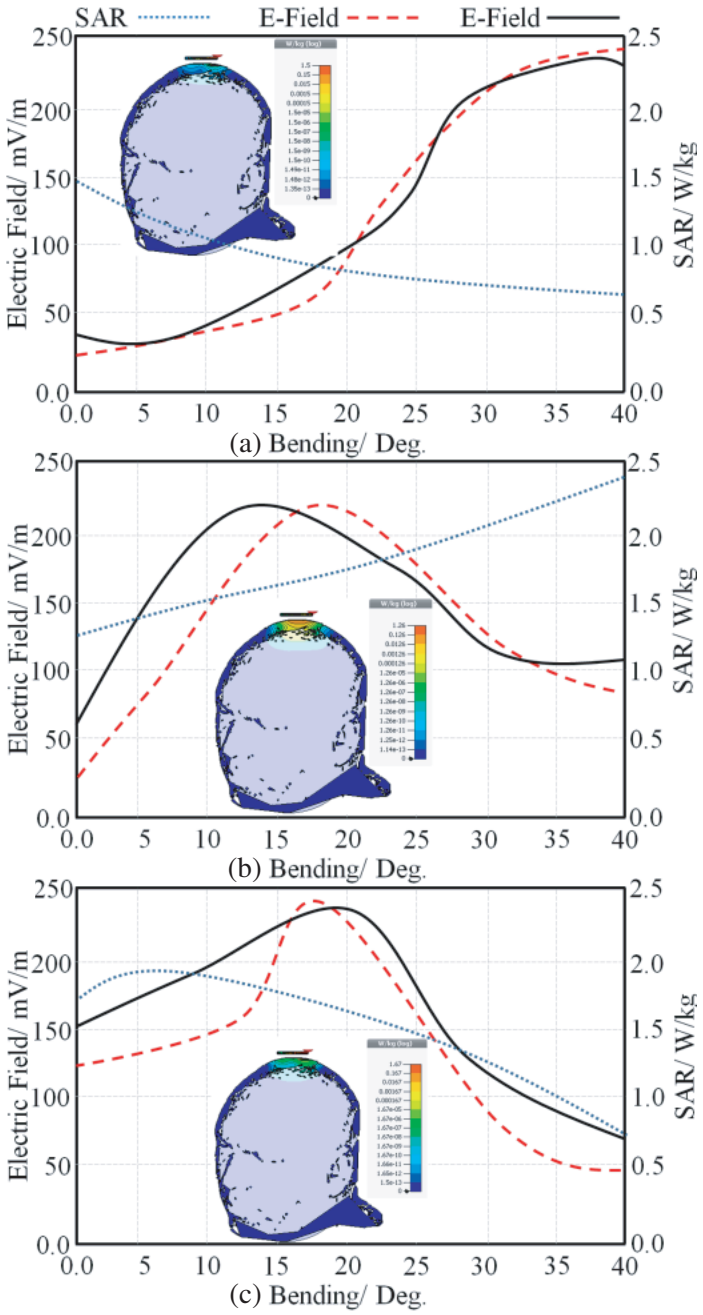

Figure 18. SAR study of the proposed antenna performance at: (a) 0.915 GHz, (b) 1.88 GHz, and (c) 2.45 GHz.

Table 4. General comparison between the proposed antenna features against other selected published work.

Ref.	Ground	Substrate	Harvested	BW	Distortion	Bending
[2]	EBG	FR4	×	UWB	√	×
[4]	Without	IPTR	×	Narrow	√	×
[5]	Without	IPTR	RF	Narrow	√	×
[6]	Without	IPTR	×	Narrow	√	×
[19]	Without	IPTR	RF	Wide	√	×
[28]	EBG	PTFE	RF	Wide	√	×
Proposed antenna	EBG	Solar panel	RF&solar	UWB	×	√

at 1.88 GHz, whereas the SAR quantity decreased significantly to 1.67 W/kg at 2.45 GHz. To conduct a study based on the concept of wearable antenna devices, a bending effect is considered numerically and experimentally on the proposed antenna over the human head. For this, the radiation leakage toward the human head is measured at different bending angles for the proposed antenna starting from 0° up to 40° with a step of 5°. Such a strategy is presented to obtain the amount of field absorption at different angels of bending when the antenna is bent over the head. The obtained measurement at 0.915 GHz realizes maximum absorption in the head at maximum angel of bending as shown in Fig. 18(a). Nevertheless, it is found that the radiation leakage decays significantly at 0° and 40° bending angles at 1.88 GHz and 2.45 GHz as depicted in Figs. 18(b) and 18(c), respectively. The SAR variations at different angles of bending are evaluated numerically. Insignificant SAR variation is observed from the results because the EBG layer area is larger than the patch area that minimizes the surface wave diffraction from the substrate edges during bending [12]. The SAR value of the proposed antenna, without bending, is compared with the SAR value for the same antenna without the EBG layer, as shown in Table 5. Significant reduction is observed in the SAR value after introducing the proposed EBG layer. The average reduction is found approximately 57.9%, 73.9%, and 71.7% at 0.91 GHz, 1.88 GHz, and 2.45 GHz, respectively.

Table 5. SAR comparison results.

Frequency/GHz	SAR/W/kg		
	Without EBG	With EBG	Reduction ratio
0.915	5.67	1.51	57.9%
1.88	8.42	1.26	73.9%
2.45	10.15	1.67	71.7%

7. CONCLUSION

In this paper, a wearable antenna is designed from a 3×5 Hilbert-shaped unit radiators patch printed on a flexible solar panel backed by EBG ground plane defects. For the antenna manufacturing, SNPs with ink printing technology are utilized for fabrication on the flexible solar panel. It is found that the proposed antenna realizes gain varied from 10 dBi up to 5 dBi over the frequency band from 0.8 GHz up to 10 GHz. When the antenna performance is numerically studied and compared with the measurements, there is a good agreement between the measured and simulated results. However, the experimental results show that the current generated from the solar panel has not been significantly affected by the antenna structure as the shaded surface of the patch is small. In addition, the measured conversion efficiency and DC output are found at approximately 90% and 1.452 V at 0.915 GHz when being connected with the rectenna port to RF with DC converter, respectively. However, the conversion efficiency is found about

49% and 60% at 1.88 GHz and 2.45 GHz, respectively. In another aspect, the addressed contributions for the proposed antenna over previous published designs are the combination of two harvesting ports based solar and RF energy in one integrated miniaturized printed antenna; this combination is the first of such type to the best of authors' knowledge. Moreover, the use of a flexible solar panel has added another feature to realize the ease of integration with wearable smart clothes systems. The SAR study demonstrates insignificant absorption effects when it is mounted close to the human body. Finally, the immunity of the proposed antenna design against the effects of physical forces such as bending effects is demonstrated when it is mounted close to the human body as wearable structure.

REFERENCES

1. Balanis, C. A., *Antenna Theory: Analysis and Design*, 3rd Edition, John Wiley & Sons Press, New York, 2005.
2. Al-Janabi, M. A. and S. K. Kayhan, "Flexible vivaldi antenna based on a fractal design for RF-energy harvesting," *Progress In Electromagnetics Research M*, Vol. 97, 177–188, 2020,
3. Shafique, K., B. A. Khawaja, M. D. Khurram, et al., "Energy harvesting using a low-cost rectenna for Internet of Things (IoT) applications," *IEEE Access*, Vol. 6, 30932–30941, 2018.
4. Elwi, T. A., "Printed microwave metamaterial-antenna circuitries on nickel oxide polymerized palm fiber substrates," *Nat. Sci. Rep.*, Vol. 9, No. 2174, 1–14, 2019,
5. Elwi, T. A., "Novel UWB printed metamaterial microstrip antenna based organic substrates for RF-energy harvesting applications," *Inter. Jour. of Elect. & Comm.*, Vol. 101, No. 9, 1–10, 2019.
6. Elwi, T. A. and B. A. Ahmed, "A fractal metamaterial based printed dipoles on a nickel oxide polymer palm fiber substrate for Wi-Fi applications," *Inter. Jour. of Elect. & Comm.*, Vol. 96, No. 23, 122–129, 2018.
7. Hatem, G. M., A. J. Salim, T. A. Elwi, et al., "Wunderlich curve fractal dipole antenna for dual-band wearable RFID applications," *Jou. Eng. and App. Scie.*, Vol. 14, No. 4, 1093–1099, 2019.
8. Zeng, M., Z. Li, A. S. Andrenko, Y. Zeng, and H. Z. Tan, "A compact dual-band rectenna for GSM900 and GSM1800 energy harvesting," *International Journal of Antennas and Propagation*, Vol. 2018, Article ID 4781465, 9 pages, 2018.
9. Elwi, T. A., A. I. Imran, and Y. Alnaiemy, "A miniaturized lotus shaped microstrip antenna loaded with EBG structures for high gain-bandwidth product applications," *Progress In Electromagnetics Research C*, Vol. 60, 157–167, 2015.
10. Elwi, T. A., "A slotted lotus-shaped microstrip antenna based EBG structures," *Wirel. Comm. Tech.*, Vol. 2, No. 1, 1–24, 2018.
11. Imran, A. I. and T. A. Elwi, "A cylindrical wideband slotted patch antenna loaded with frequency selective surface for MRI applications," *Eng. Sci. & Tech., an Int. Jou.*, Vol. 20, No. 3, 990–996, 2017.
12. Nguyen, N. H., T. D. Bui, and A. D. Le, "A novel wideband circularly polarized antenna for RF energy harvesting in wireless sensor nodes," *International Journal of Antennas and Propagation*, Vol. 2018, Article ID 1692018, 9 pages, 2018.
13. Anguera, J., C. Puente, E. Martínez, et al., "The fractal Hilbert monopole: A two-dimensional wire," *Micr. & Opt. Tech. Lett.*, Vol. 36, No. 2, 102–104, 2003.
14. Gala, D., J. Soler, C. Puente, et al., "Miniature microstrip patch antenna loaded with a space-filling line based on the fractal Hilbert curve," *Micr. & Opt. Tech. Lett.*, Vol. 38, No. 4, 311–312, 2003.
15. Azad, M. Z. and M. Ali, "A miniaturized Hilbert PIFA for dual-band mobile wireless applications," *IEEE Ant. & Wire. Prop. Lett.*, Vol. 4, No. 3, 59–62, 2005.
16. Azaro, R., F. Viani, L. Lizzi, et al., "A monopolar quad-band antenna based on a Hilbert self-affine prefractal geometry," *IEEE Ant. & Wire. Prop. Lett.*, Vol. 8, No. 5, 177–180, 2009.
17. Puente, C., E. Rozan, and J. Anguera, "Space-filling miniature antennas," US Pat. 2000, 7,202,822.

18. Mathur, R. and S. Dwari, "Compact planar reconfigurable UWB-MIMO antenna with on-demand worldwide interoperability for microwave access/wireless local area network rejection," *IET Microw. Antennas Propag.*, Vol. 13, 1684–1689, 2019.
19. Elwi, T. A., Z. A. Al-Hussain, and O. Tawfeeq, "A Hilbert metamaterial printed antenna based on organic substrates for energy harvesting," *IET Micr., Ant. & Prop.*, Vol. 10, No. 2, 1–8, 2019.
20. Vaccaro, S., C. Pereira, J. R. Mosig, et al., "In-flight experiment for combined planar antennas and solar cells (SOLANT)," *IET Micr., Ant. & Prop.*, Vol. 3, No. 8, 1279–1287, 2009.
21. Vaccaro, S., P. Torres, J. R. Mosig, et al., "Stainless steel slot antenna with integrated solar cells," *Electron. Lett.*, Vol. 36, No. 25, 2059–2060, 2000.
22. Al-Adhami, Y. and E. Ercelebi, "A plasmonic monopole antenna array on flexible photovoltaic panels for further use of the green energy harvesting," *Progress In Electromagnetics Research M*, Vol. 68, 143–152, 2018.
23. "CSTMWS," http://www.cst.com, April 2019.
24. Vaccaro, S., J. R. Mosig, and P. Maagt, "Two advanced solar antenna "SOLANT" designs for satellite and terrestrial communications," *IEEE Tran. on Ant. & Prop.*, Vol. 51, No. 8, 110–116, 2003.
25. Al-Adhami, Y. and E. Ercelebi, "Plasmonic metamaterial dipole antenna array circuitry based on flexible solar cell panel for selfpowered wireless systems," *Micr. and Opt. Tech. Lett.*, Vol. 59, No. 9, 2365–2371, 2017.
26. "HFSS," http://www.ansoft.com, April 2019.
27. https://www.powercastco.com/documentation/p21xxcsr-evb-datasheet/.
28. Elwi, T. A., D. A. Jassim, and H. H. Mohammed, "Novel miniaturized folded UWB microstrip antenna-based metamaterial for RF energy harvesting," *Int. J. Commun. Syst.*, Vol. 1, No. e4305, 1–15, 2020.
29. Okba, A., A. Takacs, and H. Aubert, "Compact flat dipole rectenna for IoT applications," *Progress In Electromagnetics Research C*, Vol. 87, 39–49, 2018.